Title	Two phase flow simulation in a channel of a polymer electrolyte membrane fuel cell using the lattice Boltzmann method
Author(s)	Ben Salah, Yasser; Tabe, Yutaka; Chikahisa, Takemi
Citation	Journal of Power Sources, 199, 85-93 https://doi.org/10.1016/j.jpowsour.2011.10.053
Issue Date	2012-02-01
Doc URL	http://hdl.handle.net/2115/48176
Type	article (author version)
File Information	JPS199_85-93.pdf

Instructions for use

Two phase flow simulation in a channel of a PEM Fuel Cell

using the Lattice Boltzmann method

Yasser BEN SALAH [*], Yutaka TABE, Takemi CHIKAHISA

Division of Energy and Environmental Systems, Graduate School of Engineering,

Hokkaido University

N13 W8, Kita-ku, Sapporo 060-8628, Japan

[*] Corresponding author. Tel.: +81 11 706 6333; fax: +81 11 706 7889.

E-mail address: yasser@eng.hokudai.ac.jp; N13 W8, Kita-ku, Sapporo 060-8628, Japan

Abstract

Water management in polymer electrolyte (PEM) fuel cells is important for fuel cell performance and durability. Numerical simulations using the lattice Boltzmann method (LBM) are developed to elucidate the dynamic behavior of condensed water and gas flows in a polymer electrolyte membrane (PEM) fuel cell gas channel. A scheme for two-phase flow with large density differences was applied to establish the optimum gas channel design for different gas channel heights, droplet positions and gas channel walls wettability. The present simulation using the LBM, which considers the actual physical properties of the system, shows the effect of the cross-sectional shape, the droplet initial position, droplet volume and the air flow velocity for both hydrophobic and hydrophilic gas channels. The discussion of optimum channel height and drain performance was made using two factors "pumping efficiency" and "drainage speed". It is shown that deeper channels give better draining

efficiency than shallower channels, and the efficiency remains largely unchanged when the droplet touches corners or the top of walls in the gas channel. As the droplet velocity, i.e. the drainage flow rate, becomes higher and the drainage efficiency becomes less dependent on droplet locations with shallower channels, shallower channels are better than deeper channels as the pumping efficiency is not greatly affected. Introducing a new dimensionless parameter, "pumping efficiency", the investigation discusses the effect of the various parameters on the drainage performance of a PEM fuel cell gas channel.

Keywords: Lattice Boltzmann method, Droplet, Dynamic behavior, PEM fuel cell, Large density difference

Nomenclature

c : characteristic particle speed (m s^{-1})

c_i : restricted velocities of particle ensembles (m s^{-1})

f_i : particle velocity distribution functions for the calculation of an order parameter

g : gravitational acceleration (m s^{-2})

g_i : particle velocity distribution functions for the calculation of a predicted velocity

H : vertical length of simulation domain (m)

I : cell current density (A m^{-2})

L : characteristic length (m)

m : droplet mass (kg)

p : pressure (Pa)

Q : gas flow rate (m^3 s^{-1})

Sh : Strouhal number

t : time (s)

t_0 : characteristic time scale (s)

Δt : time step during which the particles travel the lattice spacing (s)

$\boldsymbol{u}$: current velocity (m s^{-1})

$\boldsymbol{u}^*$: predicted velocity (m s^{-1})

U : characteristic flow speed (m s^{-1})

U_{dr} : droplet velocity (m s^{-1})

x, y, z : position coordinates (m)

Δx : spacing of the cubic lattice (m)

κ_f : constant determining the width of the interface of two phases

κ_g : constant determining the strength of the surface tension

θ : contact angle

μ : viscosity (Pa s)

ξ : coordinate perpendicular to the interface (m)

ρ : density (kg m^{-3})

ρ_0 : reference density (kg m^{-3})

σ : interface tension (N m^{-1})

τ_f, τ_g : dimensionless single relaxation time

η : pumping efficiency

ϕ : order parameter

ϕ_0 : reference order parameter

Superscript, Subscript

A   : advancing

dr   : droplet

eq   : equilibrium state

ext   : exterior

in   : inflow

int   : interior

G   : gas

L   : liquid

R   : receding

S   : solid

s   : static

sd   : difference between with and without droplet

α, β : Cartesian coordinates

1. Introduction

Phenomena involved in PEM fuel cell operation are complex; specifically, they involve heat transfer, species and charge transport, multiphase flows, and electrochemical reactions. Basic research into these phenomena is critically important to overcome two major

barriers to PEM fuel cell use, durability and cost. This paper investigates water management

which is essential for improving the performance of polymer electrolyte membrane (PEM)

fuel cells. The membrane of PEM fuel cells has to be fully hydrated to maintain high proton

conductivity, and at the same time excess water condenses in the gas diffusion layers (GDL)

or gas flow channels (GFCs) and prevents the supply of reactants to the electrodes under high

current density conditions. Phenomena related to this are generally referred to as "flooding"

and may be a cause of durability and performance reductions due to reactant starvation, and

the GDL generally uses hydrophobic materials to facilitate liquid water drainage, like in the

investigation of the LBM simulations reported here. At the cathode GDL/GFC interface,

oxygen transports towards the electrode where it reacts with protons and electrons to produce

water, which eventually enters the cell channels. The interfacial resistance to the reactant

transport will be significantly increased by the presence of liquid water here. Optical

visualization has shown that liquid water is present as droplets on the GDL surface, and is

removed by the gas flow and/or attach to the channel walls [1]. Studies have been conducted

on the liquid water behavior in channels and optimization of gas channel design. Chen et al.

[2] conducted the analysis of droplet instability and detachment and indicated that the static

contact angle (θ_s) and contact angle hysteresis (the difference between advancing and receding

contact angles, i.e., θ_A–θ_R), are both important parameters in determining the force required to

move a droplet across a surface. Instability diagrams were developed to explore the operating

conditions under which droplets become unstable, as unstable droplet conditions are desirable

to operate the fuel cell under conditions allowing the instantaneous removal of droplets from

the GDL/GFC interface so as to prevent blockage of pathways for oxygen transport to the

three-phase reaction sites. Following Chen's work [2], Kumbur et al. [3] proposed a similar analytical model to elucidate the effects of channel geometry and GDL surface properties on water droplet instability. Hao et al. [4] used the multiphase free-energy lattice Boltzmann method to study the effect of gas flow velocity and GDL wettability on water droplet dynamic behavior. Two-dimensional simulation employing the volume of fluid (VOF) method were performed to investigate the dynamic behavior of a water droplet subjected to air flow in the bulk of the gas channel [5] and to study the detachment of liquid droplets from the surfaces of porous materials used in (PEM) fuel cells, under the influence of cross-flowing air [6]. The effects of gas flow velocity and surface wettability on the two-phase flow patterns in flow channels were investigated most recently by Ding et al. [7] using the volume of fluid (VOF) method. The VOF method could include the effect of dynamic contact angle changes, which is an important parameter in the droplet dynamics in the present model. In order to obtain the dynamic change of the contact angle, a complicated numerical scheme must be used to track interface changes continuously [6], and experimental correlations for the advancing and receding contact angles with the gas velocity were employed in the VOF method [8]. The lattice Boltzmann method (LBM) is a powerful technique for simulating transport and fluid flows involving interfacial dynamics and complex geometries. In particular, due to the kinetic nature and absence of a need to track the phase interfaces, the LBM has been found very effective to simulate two-phase flow in the gas channels [9, 10]. The LBM could also estimate the relation between the dynamic contact angles and the droplet motion using the static nature of wettability without further experimental correlations (as it will be discussed later in Section 3.1).

In this paper, numerical simulation using the LBM has been developed with for conditions with large density differences, to understand the dynamic behavior of liquid water in gas channels and the effect of different parameters on the draining performance. The effect of droplet position, surface wall wettability, and channel height under a constant flow rate is also discussed.

2. Simulation Method

The LBM simulates mass and heat transport phenomena by tracking movements of particle ensembles with velocities restricted to a finite set of vectors. The particle population is expressed by distribution functions, and the time evolution of the distribution functions is calculated by the simple law of collision and transition, ensuring that the LBM obeys the continuity equation and the Navier-Stokes equations for incompressible fluids. Additionally, introducing interaction among the particle ensembles in the equations makes it possible to simulate multi-phase flow. Because of the simplicity of the algorithm, the LBM has the following advantages: flexibility for complex boundary geometries, simplicity of parallel computing, and accuracy in mass conservation. In multi-phase flows, no tracking of interfaces is necessary and the clearly distinguishable interfaces can be maintained without additional assumptions. To simulate the two-phase flow in the 3-dimensional gas channel of a PEM fuel cell, the extended LBM proposed by Inamuro et al. [11] was applied. Two-phase flows with large density differences, density ratios up to 1000, can be calculated by this method [10].

In the model, the non-dimensional variables defined by a characteristic length L, a characteristic particle speed c, a characteristic time scale $t_0 = L/U$, where U is a characteristic flow speed, a reference order parameter ϕ_0, and a reference density ρ_0 are also used [11], "non-dimensional" terms are represented by a circumflex. This paper uses a three-dimensional 15 velocities model (3D15V model) and the velocities of particle ensembles are restricted to the following vectors $\hat{\boldsymbol{c}}_i$ ($i = 1, 2, \ldots, 15$) in the 3-dimensional case as shown in Fig. 1 [12]

$$[\hat{\boldsymbol{c}}_1, \hat{\boldsymbol{c}}_2, \hat{\boldsymbol{c}}_3, \hat{\boldsymbol{c}}_4, \hat{\boldsymbol{c}}_5, \hat{\boldsymbol{c}}_6, \hat{\boldsymbol{c}}_7, \hat{\boldsymbol{c}}_8, \hat{\boldsymbol{c}}_9, \hat{\boldsymbol{c}}_{10}, \hat{\boldsymbol{c}}_{11}, \hat{\boldsymbol{c}}_{12}, \hat{\boldsymbol{c}}_{13}, \hat{\boldsymbol{c}}_{14}, \hat{\boldsymbol{c}}_{15}] =$$

$$\begin{bmatrix} 0 & 1 & 0 & 0 & -1 & 0 & 0 & 1 & -1 & 1 & 1 & -1 & 1 & -1 & -1 \\ 0 & 0 & 1 & 0 & 0 & -1 & 0 & 1 & 1 & -1 & 1 & -1 & -1 & 1 & -1 \\ 0 & 0 & 0 & 1 & 0 & 0 & -1 & 1 & 1 & 1 & -1 & -1 & -1 & -1 & 1 \end{bmatrix} \tag{1}$$

Two particle velocity distribution functions, $\hat{f}_i$ and $\hat{g}_i$, are used. The $\hat{f}_i$ function is used for the calculation of an order parameter $\hat{\phi}$ which distinguishes two phases: $\hat{\phi} < \hat{\phi}_G$ corresponding to the gas phase, $\hat{\phi} > \hat{\phi}_L$ the liquid phase, and $\hat{\phi}_G \leq \hat{\phi} \leq \hat{\phi}_L$ the condition at the interface between liquid and gas phases. The $\hat{g}_i$ function is used for the calculation of a predicted velocity for the two-phase fluid without a pressure gradient. The evolution of the particle distribution functions $\hat{f}_i$ and $\hat{g}_i$ with the velocity $\hat{\boldsymbol{c}}_i$ at point $\hat{x}$ and time $\hat{t}$ are computed by the following equations.

$$\hat{f}_i(\hat{\boldsymbol{x}} + \hat{\boldsymbol{c}}_i \Delta \hat{t}, \hat{t} + \Delta \hat{t}) = \hat{f}_i(\hat{\boldsymbol{x}}, \hat{t}) - \frac{1}{\tau_f}[\hat{f}_i(\hat{\boldsymbol{x}}, \hat{t}) - \hat{f}_i^{eq}(\hat{\boldsymbol{x}}, \hat{t})] \tag{2}$$

$$\hat{g}_i(\hat{x} + \hat{c}_i \Delta \hat{t}, \hat{t} + \Delta \hat{t}) = \hat{g}_i(\hat{x}, \hat{t}) - \frac{1}{\tau_g}[\hat{g}_i(\hat{x}, \hat{t}) - \hat{g}_i^{\ eq}(\hat{x}, \hat{t})]$$

$$+ 3E_i \hat{c}_{i\alpha} \frac{1}{\hat{\rho}} \left[\frac{\partial}{\partial \hat{x}_\beta} \left\{ \hat{\mu} \left(\frac{\partial \hat{u}_\beta}{\partial \hat{x}_\alpha} + \frac{\partial \hat{u}_\alpha}{\partial \hat{x}_\beta} \right) \right\} \right] \Delta \hat{x} - 3E_i \hat{c}_{iy} \left(1 - \frac{\hat{\rho}_G}{\hat{\rho}} \right) \hat{g} \Delta \hat{x} \qquad (3)$$

Here, $\hat{f}_i^{\ eq}$ and $\hat{g}_i^{\ eq}$ are the equilibrium distribution functions, E_i is the associated weight coefficients presented below, τ_f and τ_g are dimensionless single relaxation times, $\Delta \hat{x}$ is the spacing of the cubic lattice, $\Delta \hat{t}$ is the time step during which the particles travel the distance of the lattice spacing, $\hat{\rho}$ is the density, $\hat{\mu}$ is the viscosity, $\hat{u}$ is the current velocity, and $\hat{g}$ is the gravitational acceleration. The third and last terms on the right hand side of Eq. (3) represent the effects of viscous stress and gravitation, respectively.

The order parameter $\hat{\phi}$ distinguishing the two phases and the predicted velocity $\hat{u}^*$ of the multi-component fluids are defined in terms of the two particle velocity distribution functions as follows:

$$\hat{\phi} = \sum_{i=1}^{9} \hat{f}_i \qquad (4)$$

$$\hat{u}^* = \sum_{i=1}^{9} \hat{c}_i \hat{g}_i \qquad (5)$$

The equilibrium distribution functions f_i^{eq} and g_i^{eq} in Eqs. (2) and (3) are given by

$$\hat{f}_i^{\ eq} = H_i \hat{\phi} + F_i \left[\hat{p}_0 - \kappa_f \hat{\phi} \frac{\partial^2 \hat{\phi}}{\partial \hat{x}_\alpha^2} - \frac{\kappa_f}{6} \left(\frac{\partial \hat{\phi}}{\partial \hat{x}_\alpha} \right)^2 \right] + 3E_i \hat{\phi} \hat{c}_{i\alpha} \hat{u}_\alpha + E_i \kappa_f G_{\alpha\beta}(\hat{\phi}) \hat{c}_{i\alpha} \hat{c}_{i\beta} \quad (6)$$

$$\hat{g}_i^{eq} = E_i \left[1 + 3\hat{c}_{i\alpha}\hat{u}_\alpha - \frac{3}{2}\hat{u}_\alpha\hat{u}_\alpha + \frac{9}{2}\hat{c}_{i\alpha}\hat{c}_{i\beta}\hat{u}_\alpha\hat{u}_\beta + \frac{3}{2}\left(\tau_g - \frac{1}{2}\right)\Delta\hat{x}\left(\frac{\partial\hat{u}_\beta}{\partial\hat{x}_\alpha} + \frac{\partial\hat{u}_\alpha}{\partial\hat{x}_\beta}\right)\hat{c}_{i\alpha}\hat{c}_{i\beta} \right]$$

$$+ E_i \frac{\kappa_g}{\hat{\rho}} G_{\alpha\beta}(\hat{\rho})\hat{c}_{i\alpha}\hat{c}_{i\beta} - \frac{2}{3}F_i\frac{\kappa_g}{\hat{\rho}}|\nabla\hat{\rho}|^2 \qquad (7)$$

Where,

$$E_1 = \frac{2}{9}, E_2 = E_3 = ...E_7 = \frac{1}{9}, E_8 = E_9 = ...E_{15} = \frac{1}{72}$$

$$H_1 = 1, H_2 = H_3 = \cdots = H_{15} = 0, F_1 = -\frac{7}{3}, F_i = 3E_i (i = 2,3,\cdots,15).$$

with $\alpha, \beta = \hat{x}, \hat{y}, \hat{z}$ the subscripts α and β represent the Cartesian coordinates and the summation convention is used. In the above equations, κ_f is a constant parameter determining the width of the interface between two phases, κ_g is a constant parameter determining the strength of the surface tension, and the parameters $\hat{p}_0$ and $G_{\alpha\beta}$ are explained in Ref. [13]. The interfacial tension $\hat{\sigma}$ is obtained by the following equation.

$$\hat{\sigma} = \kappa_g \int_{-\infty}^{\infty} \left(\frac{\partial\hat{\rho}}{\partial\hat{\xi}}\right)^2 d\hat{\xi} \qquad (8)$$

Here, $\hat{\xi}$ is the coordinate perpendicular to the interface.

Because the predicted velocity $\hat{u}^*$ given by Eq. (5) does not satisfy the continuity equation ($\nabla\cdot\hat{u}^* = 0$), a correction of $\hat{u}^*$ is required. The current velocity $\hat{u}$ which satisfies the continuity equation can be obtained with the following equations.

$$Sh\frac{\hat{\boldsymbol{u}} - \hat{\boldsymbol{u}}*}{\Delta\hat{t}} = -\frac{\nabla\hat{p}}{\hat{\rho}} \tag{9}$$

$$\nabla\cdot\left(\frac{\nabla\hat{p}}{\hat{\rho}}\right) = Sh\frac{\nabla\cdot\hat{\boldsymbol{u}}*}{\Delta\hat{t}} \tag{10}$$

Here, $Sh = U/c$ is the Strouhal number and $\hat{p}$ is the pressure of the two-phase fluid; note that

this definition leads to the following relationships, $\Delta\hat{t} = Sh\Delta\hat{x}$, which is represented by $\Delta t =$

$\Delta x/c$ and means that the particles travel across the lattice space Δx during time step Δt. This

paper solved Eq. (10) using the Successive Over Relaxation (SOR) method. Details of this

model are described in a previous paper [13].

The effect of wettability is introduced by assuming the density of the solid wall as

proposed by the scheme of Seta and Takahashi [14]. Since the intermolecular force is

expressed in terms of the density of the fluid in the LBM, giving the density of solid wall

corresponds to giving the intermolecular force between liquid and solid wall. It has been

confirmed that this scheme can simulate the effect of wettability both on a flat surface as well

as at corners inside a gas channel [15].

3.   Results and Discussion

3.1.   Basic characteristics of droplets with the LBM

The Lattice Boltzmann method (LBM) for two-phase flows with large density

differences has been applied to the simulation of liquid water and air flow in a PEM fuel cell

[13]. However, there were problems with the applicability of the simulation results, e.g. there remained the issue of non conservation of the mass of liquid water. Improvements to the calculation process, the formulations for the SOR method, the derivation method of density with steep gradients, and other refinements, make a stable and reliable simulation of two-phase flows with large density differences possible [9].

To validate the present LBM model, a liquid water droplet is initially placed at the center of a 50 x 50 x 50 (in lattice units) domain without gravity and air current. According to Laplace law, when the system reaches the equilibrium condition in the absence of body force, the pressure difference between interior and exterior of the droplet, Δp, is determined by the radius of the droplet R and the surface tension σ as:

$$\Delta p = p_{int} - p_{ext} = \frac{2}{R}\sigma \qquad (11)$$

To test Laplace's law, given by Eq. (11), the simulation was conducted for several droplet radii. The change of pressure difference with respect to ($2/R$) is plotted in Fig. 2 and it exhibits good agreement with Laplace's law. The slope of the linear fit is the interfacial tension, σ, which is about 0.067 N m^{-1} for the present droplet test simulation.

Fig. 3 is a schematic outline of the domain for the calculations used in the simulations. The density ratio of liquid to gas is $\rho_L/\rho_G = 847$ ($\rho_L = 997$ kg m^{-3}, $\rho_G = 1.18$ kg m^{-3}), the viscosities of the liquid and gas are $\mu_L = 8.54$ x 10^{-4} Pa s and $\mu_G = 1.86$ x 10^{-5} Pa s, and the interfacial tension between water and air is $\sigma = 7.29$ x 10^{-2} N m^{-1}. The time step Δt is set to 2.5 x 10^{-7} s and the gravitational acceleration is $g = 0$ m s^{-2}, with other parameters $\tau_f = 1$, $\tau_g = 1$, $\kappa_f = 0.5(\Delta x)^2$, $\hat{\phi}_L = 0.092$ and $\hat{\phi}_G = 0.015$. The domain is divided into a 40 x 20 x 100

cubic cells of 0.025mm in the x, y, and z directions with the channel length 2.5 mm, which is sufficient for a single droplet simulation. The bottom of the channel corresponds to the gas diffusion layer (GDL), which is a hydrophobic surface with an equilibrium static contact angle (θ_s) of 120º and the order parameter $\hat{\phi}_S$ is equal to 0.045. The relationship between the equilibrium contact angle θ_s and the order parameter $\hat{\phi}_S$ will be discussed later. The other three walls are also hydrophobic surfaces with static contact angles of 100º ($\hat{\phi}_S = 0.050$).

The roughness of a porous medium like GDL affects the droplet movement, but this model assumes a smooth surface and so any effect of GDL roughness is ignored, like in Reference [5]. The liquid water droplet is placed either at a corner or at the center of the cell (Fig. 3 shows the case with the droplet at the corner). Gravitational forces were not considered in this simulation. A Poiseuille-like flow is given at the inlet of the channel, $z = 0$ and a free outflow condition is used at the outlet of the channel.

To evaluate the effectiveness of the LBM model here for wettability effects in the simulation, a static droplet test was performed. The static contact angle is represented by the solid wall index function $\hat{\phi}_S$, and in the present contact angle simulation, initially, a liquid droplet of radius 10 in lattice units, is placed at the geometric center of the bottom solid wall of the $40 \times 20 \times 40$ (in lattice units) computational domain. Here, only the bottom surface index function, which is in contact with the droplet, is changed. The value of $\hat{\phi}_S$ is varied until the droplet reaches equilibrium with an unchanged spherical-cap shape achieving an unchanged droplet shape with different contact angles. Fig. 4 shows two contact angles obtained by adjusting the bottom wall index function as well as the density contours of the droplet fluid at the mid-section. The obtained static contact angles for different wall index

functions are plotted on Fig. 5, showing the contact angle as a function of $\hat{\phi}_S$. Fig. 5 shows

that a higher than 0.055 value of $\hat{\phi}_S$ gives rise to a contact angle of less than 90°, indicating a

hydrophilic surface. A contact angle larger than 90° is formed when $\hat{\phi}_S$ is less than 0.055;

the $\hat{\phi}_S = 0.055$ is the neutral wetting situation.

Next, the dynamic behavior of a moving droplet placed at the center of the gas

channel was also simulated in a computational 40 x 40 x 100 cell domain with the same lattice

space interval as in the basic cell domain case. Initially a droplet at an equilibrium state is

placed at the geometric center of the bottom solid wall and moves due to the Poiseuille gas

flow with a mean velocity of $U_{in} = 0.32$ m s^{-1}. Fig. 6(a) is an enlarged view of the profile of

the moving droplet and the corresponding velocity fields. The velocity field shows the

direction and difference between the gas and droplet velocities value. The deformation of the

moving droplet and its motion on the hydrophobic surface is clearly suggested by this figure.

The corresponding mid-section of the absolute velocity profile is plotted in Fig. 6(b). The

location of $y/H = 0.4$ corresponds to the top of the droplet. The effect of the flow velocity on

the dynamic contact angle was also studied. Fig. 7 shows simulated droplet shapes at different

gas flow velocities for the basic case, where the initial static shape of the droplet is shown to

be a truncated sphere (Fig. 7 "initial"). It clearly shows that droplet deformation increases as

the average gas flow velocity U_{in} increases due to the increases in the drag force acting on the

droplet. For higher flow velocities, the droplet is continuously deformed and displays a

growing top and spreading out as especially shown for the case of $U_{in} = 0.8$ m s^{-1}, this

deformation will lead to droplet instability, and so easier water removal from the channel.

The droplet movement induces different advancing and receding contact angles, θ_A and θ_R. Fig. 8 presents the results of the LBM simulations for the contact angle hysteresis, $\cos \theta_R - \cos \theta_A$, as a function of the droplet velocity U_{dr} for steady conditions. The contact angle hysteresis increases with increases in U_{dr}. The dependence is close to linear which is in good agreement with the work of Hao et al. [16] based on a macroscopic force balance analytical analysis. The simulated linear functional dependence between the contact angle hysteresis and droplet terminal velocity was also observed by the experiments by Kumbur et al. [3]. This shows a partial validation of the model within the limited available data. It should be noted that the LBM can estimate the relation between the contact angle hysteresis and the droplet motion without any experimental data about the dynamic contact angle of the moving droplet.

Fig. 9 shows the changes in the movement of the center of gravity of a liquid water droplet along the channel and the pressure drop in the air flow in a 1.0 mm wide channel for the basic case (detailed in 3.1). The air flow rate is equal to 24 SCCM (Standard Cubic Centimeters per Minute). This value is very similar to an actual fuel cell under the following operation conditions: cell current density $I = 0.5$ A cm^{-2}, active area of 2 cm^2 for one 100 mm long channel, and a stoichiometric ratio of about 1.4. The initial droplet position is at the center. The gas mean flow velocity U_{in} is 0.8 m s^{-1}, and the time step is 2.5 x 10^{-7} s. Fig. 9 shows that the velocity of the liquid water droplet, which corresponds to the gradient of the moving distance, and the pressure drop of air flow reach steady values. The terminal droplet velocity and the pressure of the air flow will be used for the evaluation of the draining performance in the following.

3.2. Evaluation of draining performance

3.2.1 Effect of channel height

The simulations of droplet behaviors for droplets of different sizes placed at the center of the hydrophobic bottom wall were performed for different channel heights in channels with the same width and for one gas flow rate corresponding to the basic condition with a gas inlet velocity U_{in} is 0.8 m s^{-1}. Here, for larger droplet volumes, the droplet touches the top wall for shallow channels $H = 0.4$ mm and 0.5 mm, and for deeper channels $H = 0.7$ mm and 1.0 mm the droplet touches the two side walls of the gas channel. In Fig. 10, the cases where the droplets touch the top wall are marked with a circle O and droplets touching the two side walls are marked with a dashed square ⬚. Fig. 10(a) shows the changes in the droplet terminal velocity, U_{dr} vs. the droplet volume for channel heights of 0.4 mm to 1.0 mm. As the water droplet size in the channel increases, the droplet terminal velocity also increases. When the droplet touches the top wall or the side walls, the terminal velocity decreases due to the resistance arising from the wall. The decrease in terminal velocity of the droplets will cause an increase of air flow pressure. The pressure drop in the gas channel is analyzed in terms of p_{sd} (the difference of actual pressure drop with a droplet present and the pressure drop without droplets). The results of the pressure drop in the gas channel are plotted on Fig. 10(b). Comparing the cases where droplets either touch the top wall or the side walls, show that, for the same droplet mass, deeper channels result in a lower pressure drop.

After analyzing the droplet velocity and the pressure drop, we introduced a "pumping efficiency parameter", η, defined as follow;

$$\eta = \frac{m_{dr} g U_{dr}}{p_{sd} Q} \tag{12}$$

Here, Q is the gas flow rate and m_{dr} is the liquid droplet's mass. When we consider the frictional work of moving a droplet at a velocity of U_{dr}, the power is proportional to $m_{dr} g U_{dr}$. Thus the pumping efficiency has a meaning of droplet moving power relative to the pumping work. In other words, this is related to the parameter inversely proportional to the effective friction coefficient. Larger pumping efficiency indicates smaller equivalent friction coefficient, and it corresponds to the better water removal ability for the same compressor work. In general, a low pressure difference across the flow field is desired because of lower auxiliary energy demand, e.g. for air compression. The pumping efficiency is plotted vs. droplet size in Fig. 10(c). The plots show two regions; the first corresponds to the case when the droplet does not touch side walls or top wall and the second region is for the case where the droplet touches the top wall or the two side walls of the gas channel. When the droplet does not touch the walls, the pumping efficiency increases with increases in channel height leading to a slowing of the speed of the droplet since the flow rate of the gas is constant. For the second region, where the droplet touches the top wall, for $H = 0.4$ mm and $H = 0.5$ mm, the pumping efficiency is only little affected by the touching of the top wall effect. However, when the droplet touches the side walls in the deeper gas channels, $H = 0.7$ mm and $H = 1.0$ mm, the pumping efficiency is dramatically decreased because of the higher resistance exerted by the

two side walls on the droplet motion and the pumping efficiency becomes similar to the case where the droplet touches to the corner or the top wall. Considering these results, the channel height of 0.5 mm may be concluded to be superior for draining the droplets since the drainage speed is also high. This optimum channel shape was also reported in the experimental work of Akhtar et al. from a different viewpoint [17]. They concluded from the experiments of a droplet detachment in a channel that the rectangular shaped channel with a width of 1 mm and a depth of 0.5 mm is found to exhibit best water removal properties at a reasonable pressure drop.

3.2.2 Effect of droplet position

The initial droplet position is also an important factor in the pump work, and the simulation of the water behavior, where the droplet is placed at the corner of the channel is shown in Fig. 11(a), and shows remarkable differences from the droplet velocity values of the case when droplet is placed at the center (Fig. 10(a)). When the droplet is placed at the corner, the water droplet is subject to a high resistance from the contact walls and it is far from the Poiseuille flow mainstream (center of the channel where the velocity is the highest). In this situation, the droplet velocity is much slower, which explains the large differences between Fig. 10(a) and Fig. 11(a). For larger droplet sizes and when the droplet is placed at corner and touching the top wall, the terminal droplet velocity is slightly increased due to the larger volume and as more of the droplet volume is nearer the gas channel center and mainstream flow, which results in a larger pressure drop and the pumping efficiency increases slightly as

shown in Fig. 11(b). Increasing the droplet mass further changes the droplet shape to a liquid water film.

3.2.3 Effect of wettability

In this study, the wettability effect is considered in the index function of the solid wall. The dynamic simulation for both hydrophobic and hydrophilic separators (static contact angle 60°, $\hat{\phi}_S = 0.060$) and the bottom surface, which corresponds to the GDL hydrophobic as in previous simulations, was conducted for the case when the droplet is placed at the corner of the gas channel. Fig. 12(a) displays the droplet terminal velocity change with droplet mass for deeper and shallower channels, $H = 1.0$ mm and $H = 0.4$ mm, for both the hydrophobic and hydrophilic cases when the droplet is placed at a corner. For both the deeper and shallower channels, the droplet velocity is relatively high for a hydrophobic channel walls than for a hydrophilic walls. The corresponding pumping efficiencies are plotted in Fig. 12(b). It shows that in the shallow gas channel, the pumping efficiency is less affected by the wettability and the droplet is able to maintain a relatively high velocity that will result in a high "drainage speed". In both two cases a hydrophobic separator gives the larger pumping efficiency.

Fig. 13 shows a three dimensional views of droplet behavior placed at corner of an initial radius of 16 lattice unites and a channel height of 0.4 mm for both hydrophobic and hydrophilic channel walls. In this case the droplet touches the top wall. Fig. 13 shows that for the hydrophilic separator case the droplet attaches to the top wall and the contact area with

GDL is smaller than with the hydrophobic separator. This is very advantageous for the fuel cell performance. A minimum bottom liquid contact area makes more space available for the gas diffusion.

3.3. Design concept

Understanding the basic phenomena and dynamic behavior of a liquid water droplet in a single gas channel here should be extended to more complex and larger scale fuel cell simulation like Reference [18]. This section presents some discussion about the application of the simulation results for design concept of a fuel cell channel. In the large scale channel, a drained moving droplet unites with other droplets, grows larger and fills with the channel. The plugging induces a drastic increase in pressure drop of the air flow, but the droplet is drained immediately with similar velocity to the air flow. Therefore, it is important that the droplet is moved before the plugging with high velocity, high pumping efficiency and small contact area with the GDL. The simulation results showed that the droplet velocity with shallower channels is kept higher and the pumping efficiency becomes less dependent on the droplet locations with shallower channels as the droplet volume increases. This may lead to the same conclusion in large scale channels that shallower channels with about 0.5 mm height are superior to deeper channels. It was also shown that a hydrophilic channel wall, relative to the GDL wall, is better for minimum liquid contact area with the GDL for larger droplet volume.

4. Conclusions

The paper investigates water droplet behavior in fuel cell channels with the same width at the same gas flow rate condition, but for different gas channel heights, droplet positions and gas channel wall wettability, using LBM simulation. The water drainage performance can be characterized by the two parameters water flow rate and pump work, which are expressed by the droplet velocity and pumping efficiency in the paper. The results obtained in the analysis may be summarized as follows:

1. Droplet velocity significantly decreases when the droplets touch to the corners or the top wall compared to the case where the droplet locates on the center of the GDL surface without touching the side or top walls.

2. Deeper channels give better drain efficiency than shallower channels, but the efficiency differences become small when the droplet touches to the corner or the top wall. As the droplet velocity, i.e. the draining flow rate, becomes higher and the pumping efficiency becomes less dependent on the droplet locations with shallower channels, shallower channels are superior to deeper channels when the pump work involved are similar.

3. Compared to hydrophobic channel walls, hydrophilic walls may result in better gas transport characteristics, as the liquid water is drawn up on the channel wall from the GDL surface to leave more open area available for gas transport to the GDL. Hydrophilic walls result in a larger pressure drop and lower draining flow rates than hydrophobic walls, however, the differences are smaller with shallower channels.

5. References

[1]   Chen KS et al. Final report on LDRD project: elucidating performance of proton-exchange-membrane fuel cells via computational modeling with experimental discovery and validation, in SAND2006-6964, Sandia Technical Report; 2006.

[2]   K.S. Chen, M.A. Hickner and D.R. Noble, Int J Energy Res 29 (12) (2005) 1113-1132.

[3]   E.C. Kumbur, K.V. Sharp and M.M. Mench, J. Power Sources. 161 (2006) 333-345.

[4]   L. Hao, P. Cheng, J. Power Sources 190 (2009) 435-446.

[5]   X. Zhu, P.C. Sui, N. Djilali, J. Power Sources 172 (2007) 287-295.

[6]   A. Theodorakakos, T. Ous, M. Gavaises, J.M. Nouri, N. Nikolopoulos, H. Yanagihara, J. of Colloid and Interface Science 300 (2006) 673-687.

[7]   Y. Ding, H.T. Bi, D.P. Wilkinson, J. Power Sources 196 (2011) 6284-6292.

[8]   B.A. Nichita, I. Zun and J.R. Thome, Proceedings of the 7th Internaional Conference on Multiphase Flow, Tampa (2010).

[9]   Y. Tabe, Y. Lee, T. Chikahisa, M. Kozakai, J. Power Sources 193 (2009) 24–31.

[10]   P.P. Mukherjee, C.Y. Wang, Q. Kang, Electrochimica Acta 54 (2009) 6861‑6875.

[11]   T. Inamuro, T. Ogata, S. Tajima, S. Konishi, J. Comput. Phys. 198 (2004) 628-644.

[12]   S. Succi, The Lattice Boltzmann Equation for Fluid Dynamics and Beyond, Oxford Science Publications, New York, 2001.

[13]   T. Ochi, K. Kikuta, Y. Tabe, T. Chikahisa, Proceedings of the 6th KSME-JASME Thermal and Fluid Engineering Conference (2005) [1/1 (CD-ROM) JJ-05] 1-4.

[14] T. Seta, R. Takahashi, Proceedings of the 14th Computational Engineering Conference, Sapporo, No. 01-10 (2001) 541-542.

[15] Y. Tabe, T. Ochi, K. Kikuta, T. Chikahisa, H. Shinohara, Proceedings of FUELCELL2005 3rd International Conference on Fuel Cell Science, Engineering and Technology, [1/1 (CD-ROM) 74172] (2005) 1-6.

[16] L. Hao, P. Cheng, Int. J. of Heat and Mass Transfer 53 (2010) 1243-1246.

[17] N. Akhtar, A. Qureshi, J. Scholta, C. Hartnig, M. Messerschmidt and W. Lehnert, Hydrogen Energy (2009) 3104-3111.

[18] V. Gurau, J. Mann, J. Electrochem. Soc., 157 (4) (2010) B512-B521.

Fig. 1.   Lattice structure of the three-dimensional D3Q15 LBM.

Fig. 2.   Droplet test confirming Laplace's law for pressure difference.

Fig. 3.   Model for calculating the behavior of a liquid water droplet in a gas channel.

Fig. 4.   Wettability change with different solid wall index functions (a) $\hat{\phi}_S = 0.045$, $\theta_s = 120°$; (b) $\hat{\phi}_S = 0.060$, $\theta_s = 70°$.

Fig. 5.   Calculated static contact angle with wall index function.

Fig. 6.   Velocity profiles: (a) View of the profile of the moving liquid droplet and the corresponding relative air flow velocities, (b) the corresponding cross-section of the absolute velocity profile.

Fig. 7.   Droplet behaviors for different mean air flow velocities.

Fig. 8.   Plot of the contact angle hysteresis vs. droplet velocity relation, showing a good agreement with Ref. [3,16].

Fig. 9.   Moving distance of a liquid water droplet and the pressure drop in the gas flow.

Fig. 10. Changes in (a) droplet terminal velocities, (b) pressure drop and (c) pumping efficiency for different droplet masses with different channel heights.

Fig. 11. Changes in (a) droplet terminal velocities, (b) pumping efficiency at corners for different droplet masses with different channel heights.

Fig. 12. Changes in (a) droplet terminal velocities, (b) pumping efficiency for hydrophobic and hydrophilic channel walls for a droplet at a corner $H = 0.4$ mm and 1.0 mm for different droplet masses.

Fig. 13. A three-dimensional view of a droplet (radius 14 lattice unites) $H = 0.4$ mm, (a) with hydrophobic channel walls and (b) hydrophilic channel walls.

Fig. 1

Fig. 2

Fig. 3

(a)

(b)

Fig. 4

Fig. 5

(a)

(b)

Fig. 6

initial

U_{in} = 0.1 m/s

U_{in} = 0.3 m/s

U_{in} = 0.5 m/s
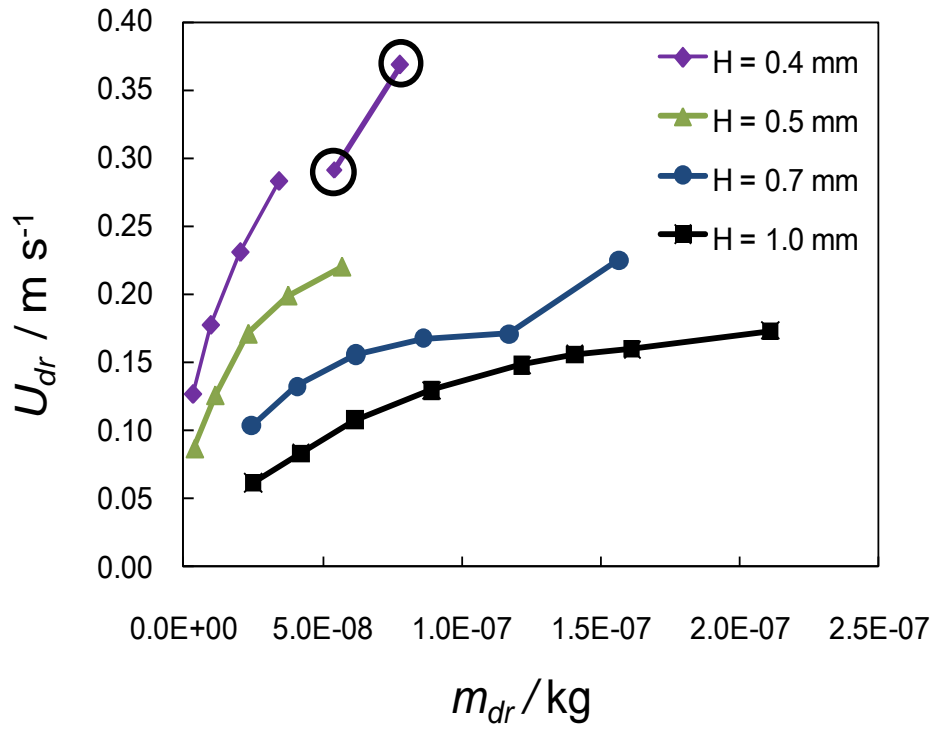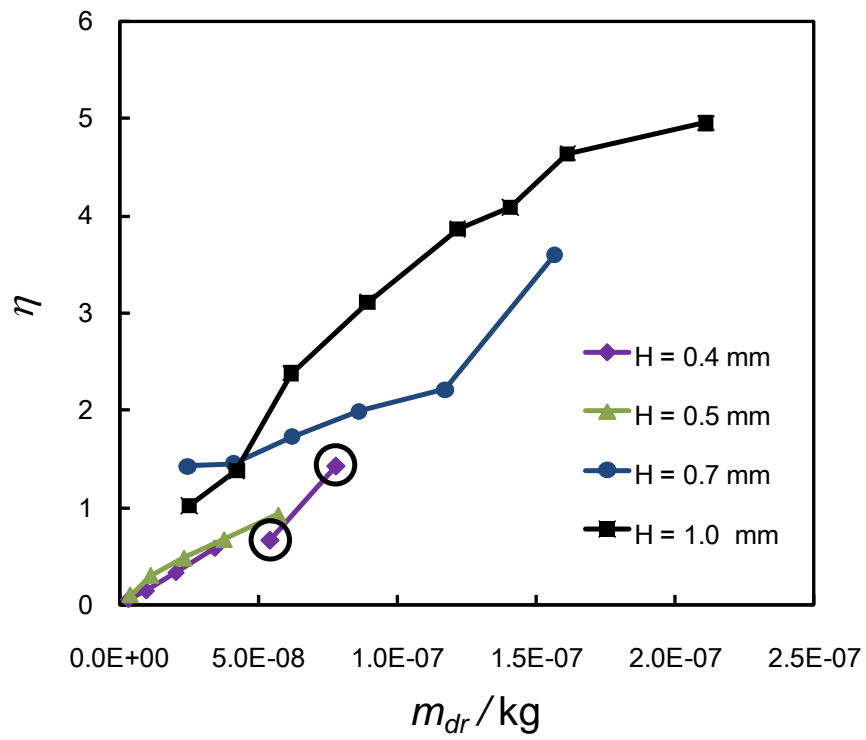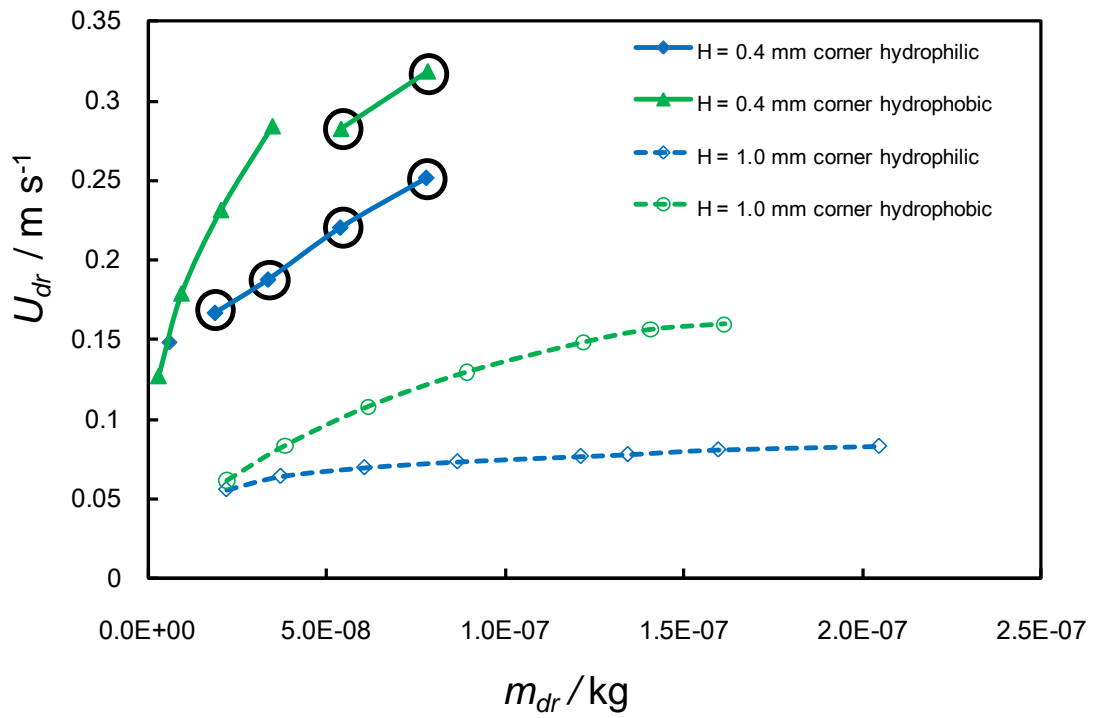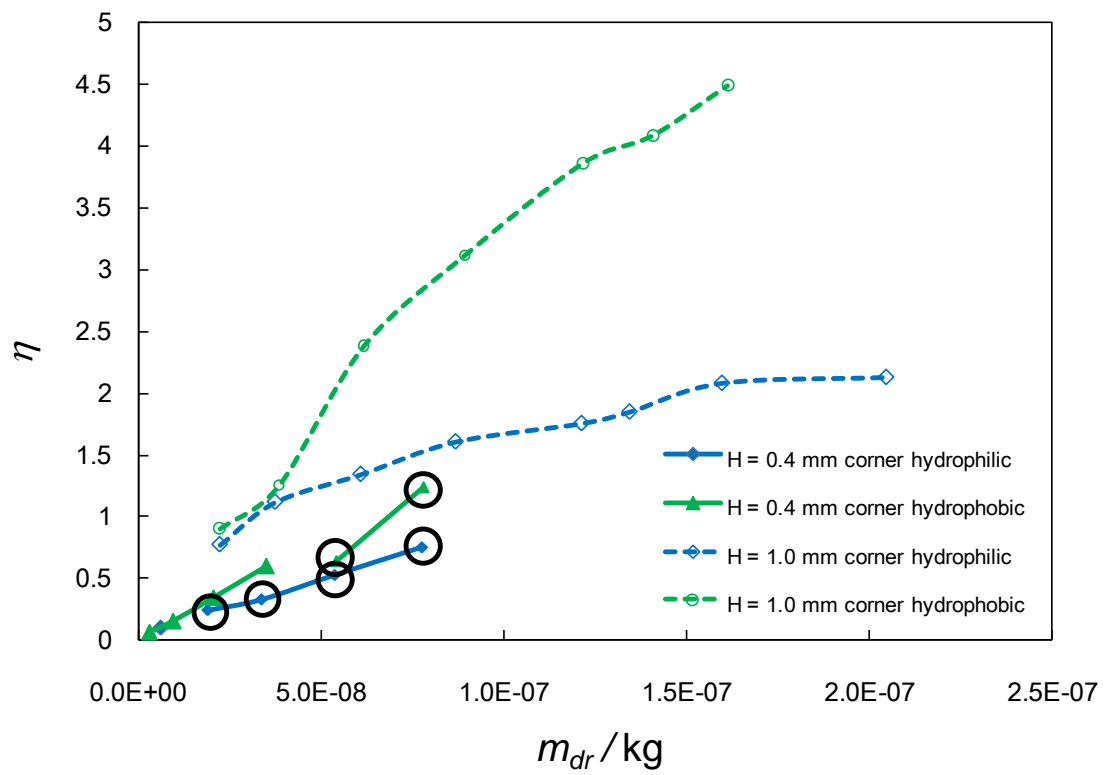
U_{in} = 0.8 m/s

Fig. 7

Fig. 8

Fig. 9

(a)

(b)

Fig. 10

(a)

(b)

Fig. 11

(a)

(b)

Fig. 12

(a)

(b)

Fig. 13